Materials and Design 169 (2019) 107672

Contents lists available at ScienceDirect

Materials and Design

journal homepage: www.elsevier.com/locate/matdes

A cellular automaton finite volume method for microstructure evolution during additive manufacturing

Yanping Lian[a,*], Zhengtao Gan[b], Cheng Yu[b], Dmitriy Kats[b], Wing Kam Liu[b], Gregory J. Wagner[b,*]

[a] Institute of Advanced Structure Technology, Beijing Institute of Technology, Beijing, China
[b] Department of Mechanical Engineering, Northwestern University, Evanston, IL, USA

HIGHLIGHTS

- A 3D cellular automata finite volume method for additive manufacturing is presented, including an enriched nucleation model
- The grain structure in the Directed Energy Deposition of IN718 alloy is simulated by the proposed method
- The effects of the processing parameters on the resulting grain structure of IN718 alloy are elaborated via the simulation
- Sandwich- and zig-zag patterns of grain structure observed in experiments are captured and explained by the proposed model

GRAPHICAL ABSTRACT

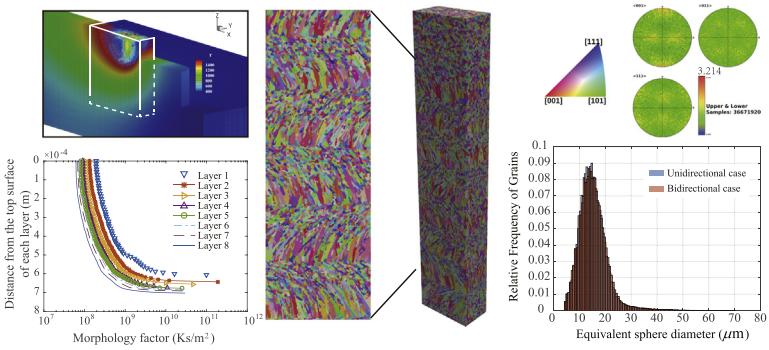

ARTICLE INFO

Article history:
Received 29 December 2018
Received in revised form 7 February 2019
Accepted 21 February 2019
Available online 5 March 2019

Keywords:
Additive manufacturing
Solidification
Grain structure
Cellular automaton
Finite volume method

ABSTRACT

Additive manufacturing (AM) processes produce unique microstructures compared with other manufacturing processes because of the large thermal gradient, high solidification rate and other local temperature variations caused by the repeated heating and melting. However, the effect of these thermal profiles on the microstructure is not thoroughly understood. In this work, a 3D cellular automaton method is coupled to a finite volume method to predict the grain structure of an alloy, e.g. Inconel 718, fabricated by AM. The heat convection due to thermocapillary flow inside the melt pool is resolved by the finite volume method for a real and accurate temperature field, while an enriched grain nucleation scheme is implemented to capture epitaxial grain growth following the mechanism identified from experiments. Simulated microstructure results are shown to be in qualitative agreement with experimental result and the effects of the process parameters on both thermal characteristics and the grain structure are identified. The 3D cellular automaton finite volume method results establish our approach as a powerful technique to model grain evolution for AM and to address the process-structure-property relationship.

1. Introduction

Metal-based additive manufacturing (AM) refers to the technology of producing 3D components by melting metal powders layer-by-layer using a focused laser or electron beam heat source. AM is an exciting technology because it can be used for rapid fabrication of near net shape components with precise geometric control and

* Corresponding authors.
E-mail addresses: yanping.lian@bit.edu.cn (Y. Lian), gregory.wagner@northwestern.edu (G.J. Wagner).

https://doi.org/10.1016/j.matdes.2019.107672

local property variations. However, AM features successive layers leading to repeated heating and melting and complex multi-physics phenomena such as laser-material interaction, thermocapillary flow, solidification, phase transformation and trapped gas bubbles. Thus, AM parts are plagued by defects and microstructure variations throughout the part. This is complicated by the various process parameters and the different AM build techniques that also influence the microstructures formed. Thus, there is a need to understand the influence of the process parameters on the microstructure formed if additively manufactured parts are to be used widely.

There are two general categories of powder-based AM techniques, differing in their method for powder delivery: Directed Energy Deposition (DED) and Powder Bed Fusion (PBF). In DED, the powder is transported directly into the molten pool at the surface by means of a carrier gas stream through a nozzle along with a coaxial heat source; one example of this method is Direct Metal Deposition (DMD), for which a laser is the most common heat source. In PBF, a heat source is rastered across a bed of powder to locally melt and solidify material; one example is selective electron beam melting (SEBM). Among many factors, the as-built microstructure plays an important role in determining the mechanical property of the build part. The grain structures formed during AM, along with the resulting mechanical properties, may show high anisotropy [1] or significant difference from their cast or wrought counterparts; these features are of both academic and industrial interest [2].

Inconel 718 (IN718) is one of the most common material systems produced by AM, and is widely used in aircraft engine and aerospace applications. In this work, we focus on the prediction of as-built primary grain (γ) structure of the IN718 alloy during the DED process. Generally, the grain structure is determined by the solidification process dictated by the process parameters, such as the laser power, laser scan speed, and raster pattern. As a result of a variety of combinations of these parameters, drastic variability at the microstructural level can be yielded in AM processes. A common feature of the resulting heterogeneous grain structure is a mixture of columnar and equiaxed grains. For example, in the experimental work by Amato et al. [3], a columnar microstructure was found in the build of IN718 alloy fabricated by selective laser melting; Liu et al. [4] have reported that the as-built microstructure of a directed laser fabricated IN718 alloy is composed of columnar grains growing epitaxially along the deposition direction; Parimi et al. [5] observed a mixture of coarse and fine grains in each layer of IN718 alloy with lower laser power, while columnar grains were found to grow epitaxially from the previously deposited layer at higher laser powers. Therefore, it is critical to understand the influence of the process parameters on the microstructure of builds in detail in order to predict and control mechanical properties by tailoring the grain structure, such as through use of optimal process parameters, or through special treatment of the input powders (e.g. adding nanoparticles to control nucleation [6]).

While traditional experimental approaches to understanding influences on microstructure are expensive and time consuming, numerical methods offer an effective means of exploring the effect of a wide range of process parameters. There are many different numerical methods to simulate the evolution of grain structure [7-10]. Among them, the phase field method (PFM) [9] and cellular automaton (CA) model [7] are two prominent approaches. PFM resolves the phase types by discretizing the differential equations that govern the evolution of phase field variables that vary smoothly across a diffuse interface region to demarcate different phases. When the PFM is used to model the grain evolution, a governing equation is solved for each grain. The PFM can model solidification at the scale of the dendrite arms by solving the phase field equations coupled to a concentration equation. Although the PFM is valuable in elucidating fine details of solidification structures, the small length scales and small numbers of grains attainable using PFM make it difficult to predict the microstructure at sizes that can be directly tied to the performance of resulting materials. In the CA model, the nucleation of grains is modeled stochastically based on a heterogeneous nucleation model associated with the local undercooling of liquid cells; the grain is modeled at the scale of the dendrite arms and grows according to a dendrite growth model in the form of a physically-based kinetic growth laws. Compared with the PFM, the CA method cannot capture fine details of the dendrite network, but requires less computer resources and therefore allows for simulations of a large numbers of grains within domains at the millimeter scale.

The CA models initially proposed by Rappaz and Gandin [7,11] for modeling solidification during casting have been used increasingly for AM. Yin and Felicelli [12] applied a 2D CA model to simulate dendritic growth during laser-engineered net shaping deposition of a single layer of Fe-C alloy. Zhang et al. [13] used a 2D CA model to predict the grain morphology during the solidification of direct metal deposition of the Ti-6Al-4 V alloy with laser melting. Rai et al. [14] proposed a 2D CA model to study the epitaxial grain structure evolution of the IN718 alloy during the SEBM process, and predicted only columnar grains. While these 2D simulation results can be generalized to 3D with stereological interpolations, the true grain sizes and shapes are uncertain. Therefore, 3D prediction is necessary to enable a higher fidelity characterization of the grain morphology. Most recently, Dezfoli et al. [15] and Panwisawas et al. [16] utilized 3D CA models for microstructure prediction and control of Ti-6Al-4 V alloys during AM processes, where only a single layer case was conducted. Koepf et al. [17] predicted the microstructure of IN718 alloy during SEBM for multiple layers, where the heat input was calculated using an analytical solution of the transient heat conduction equation. Li and Tan [18] numerically investigated the effects of nucleation mechanisms on the 3D grain structure of stainless steel 304 during the direct laser deposition process using a combination of the CA model and a thermal diffusion model. Currently, no work has been done to predict the 3D grain structure evolution during the DED process for IN718 alloy with multiple layers and different combinations of process parameters. Multi-layer builds have different microstructures from single-pass builds, so it is valuable to explore the effect of process parameters and build patterns on the grain characteristics.

In this work, we propose a 3D cellular automaton finite volume method to study the problem described above. In this method, the cellular automaton method is able to predict columnar, equiaxed and mixed grains, which are observed in the experiments conducted by Parimi et al. [5]. Meanwhile, the finite volume method is used to resolve the thermo-fluid flow field inherent to the DED process; a similar computational fluid model has been used by Manvatkar et al. [19] and Gan et al. [20] to simulate the heat transfer and melt pool dynamics for the DED process. Based on this method, we first examined the effects of laser scan speed and laser power on the grain size and morphologies for single scan track builds. Furthermore, the grain growth during the multiple layer deposition process with different raster patterns is presented and the simulation results are compared to the experimental findings [5] showing a qualitative agreement. Statistics on the distributions of grain sizes, crystal orientations, grain shape orientations, and aspect ratios are analyzed.

The rest of the paper is organized as follows. In Section 2, the governing equations for the heat transfer and thermocapillary flow models for DED are given, along with the finite volume method (FVM) discretization. In Section 3, the 3D CA method with an enriched nucleation model is introduced in detail, which is proposed to take into account both epitaxial grain growth and bulk nucleations during solidification under a unified framework, followed by the coupling method between FVM and CA in Section 4. The effects of laser power, scan speed, and raster pattern are studied in Section 5 with the proposed method. Finally, conclusions and perspectives are given in Section 6.

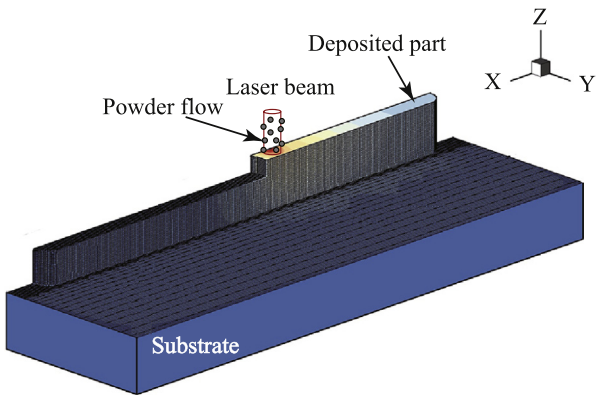

Fig. 1. A schematic of the directed energy deposition.

2. Thermocapillary flow model

2.1. Problem description

A typical DED process is illustrated in Fig. 1, where a half model is considered because of the assumed geometrical symmetry of the problem studied in this work. Specifically, thermal gradients and out-of-plane flow are assumed to be zero on the *XZ* symmetry plane. The melted metal powder is deposited on the previous layer in accordance to the predefined raster pattern with a given laser scan speed and laser power, while the surface of the built part grows as material is deposited.

2.2. Governing equations

As described in the Introduction, in metal-based AM the melting and solidification of the feed powder particles is a multi-scale and multi-physics problem. In this work, a macro-scale homogeneous model is used to describe the dominant physics including heat transfer and thermocapillary flow. The model is further simplified based on several assumptions as used by Manvatkar et al. [19] as follows:

1. The individual densities of the solid and liquid metals are assumed to be constant;
2. The top surface of the deposited layer is flat; and
3. Vaporization is ignored.

The governing equations in the Eulerian description for the heat transfer and thermocapillary flow model are given as follows [20]:

Continuity equation:

$$\frac{\partial \rho}{\partial t} + \frac{\partial(\rho u_i)}{\partial x_i} = 0 \tag{1}$$

where the subscripts i and j represent the spacial indices, ρ is the density, and u_i is the velocity. The Einstein summation convention is employed where repeated indices appear.

Momentum equations:

$$\frac{\partial \rho u_i}{\partial t} + \frac{\partial(\rho u_i u_j)}{\partial x_j} = -\frac{\partial p}{\partial x_i} + \frac{\partial \tau_{ij}}{\partial x_j} - K_0 \frac{(1-f_l^2)}{f_l^3 + B} u_i + \rho g_i \beta (T - T_{ref}) \tag{2}$$

Here p is pressure; the third term on the right hand side of Eq. (2) is the Darcy term that constrains the velocity in the mushy zone and the solid; K_0 is the morphology parameter of the porous media of the mushy zone and set to 1.6×10^4 Pa ·s ·m $^{-2}$; B is a small number to avoid division by zero and set to 1×10^{-3} [21]; g is the gravitational acceleration; β is the thermal expansion coefficient; and T_{ref} is the reference temperature. The final term on the right hand side is from the Boussinesq approximation for buoyancy [20]. Shear stress is denoted by $\tau_{ij} = \mu(u_{i,j} + u_{j,i})$ under the assumption of incompressible flow, where μ is dynamic viscosity and the comma denotes partial spatial derivative. The fluid mass fraction, f_l, is formulated as:

$$f_l = \begin{cases} 1, & T > T_l \\ \frac{T - T_s}{T_l - T_s}, & T_s \le T \le T_l \\ 0, & T < T_s \end{cases} \tag{3}$$

where T_l and T_s are the liquidus temperature and solidus temperature, respectively.

Energy equation:

$$\frac{\partial(\rho h)}{\partial t} + \frac{\partial(\rho u_i h)}{\partial x_i} = \frac{\partial}{\partial x_i}\left(\frac{k}{c_p}\frac{\partial h}{\partial x_i}\right) - \frac{\partial(\rho L f_l)}{\partial t} - \frac{(\rho u_i L f_l)}{\partial x_i} \tag{4}$$

where h is the enthalpy, c_p is the specific heat, k is the thermal conductivity, and L is the latent heat. Since there is a phase change during the melt pool evolution, the thermo-physical properties above are determined as

$$c_p = f_s c_{ps} + f_l c_{pl} \tag{5}$$

$$\rho = f_s \rho_s + f_l \rho_l \tag{6}$$

$$k = \left(\frac{\phi_s}{k_s} + \frac{\phi_l}{k_l}\right)^{-1} \tag{7}$$

Here the subscripts s and l indicate the variable for the solid phase and liquid phase, respectively. The volume fraction is represented by ϕ. Note that $\phi_s + \phi_l = f_s + f_l = 1$.

Boundary conditions (BCs) are needed for the momentum and energy equations particularly at the metal/gas interface. In the liquid region, the surface force **F** includes surface tension and thermocapillary forces:

$$\mathbf{F} = \sigma\kappa\mathbf{n}^{\star} - \nabla_s T \frac{\mathrm{d}\sigma}{\mathrm{d}T} \tag{8}$$

where σ is the surface tension coefficient, κ is the curvature, $n^{\star}$ is the normal of the liquid surface pointing into the liquid phase, and ∇_s denotes the surface gradient on the interface. Since the flat-surface assumption is used, κ is set to zero, which means that the normal component of the surface tension is neglected. Furthermore, it is assumed that the derivative of surface tension with respect to temperature is a constant value assumed to be 2×10^{-5} N·m^{-1}·K^{-1} [22].

Energy equation BCs consist of thermal convection (q_C) and thermal radiation (q_R) fluxes at the exposed surface:

$$q_C = -h_c (T - T_{ref}) \tag{9}$$

$$q_R = -\hat{\sigma}\epsilon\left(T^4 - T_{ref}^4\right) \tag{10}$$

where the heat transfer coefficient h_c is set to 100 W m^{-2} K^{-1} in this work to account for the strong convection caused by the shield gas flow used in DED; $\hat{\sigma}$ is the Stefan-Boltzmann constant; and ϵ is the emissivity. Moreover, we treat the laser heat source used in the AM process as a time-dependent heat flux BC on the surface, defined by:

$$q = \frac{2Q(1-\eta_p)\eta_l}{\pi r_b^2} \exp\left(\frac{-2((x - V_s t)^2 + y^2)}{r_b^2}\right) \tag{11}$$

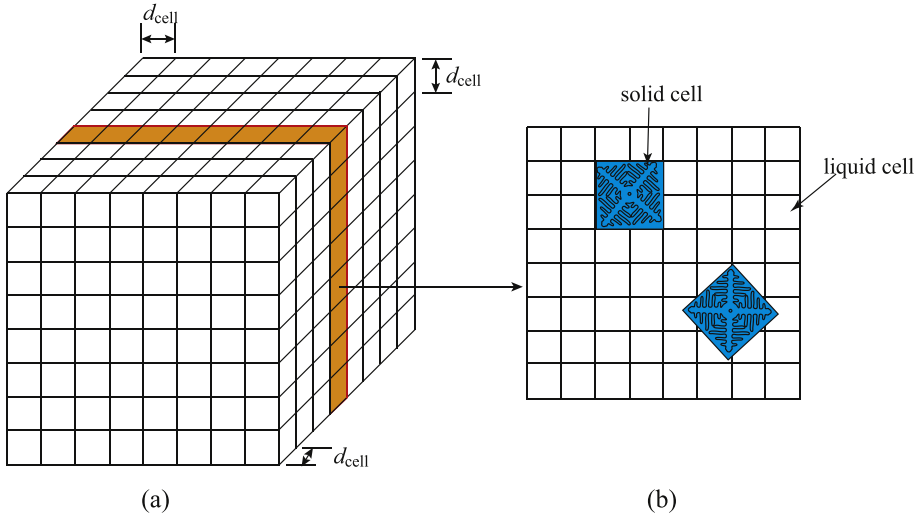

Fig. 2. (a) A 3D cellular automaton network to predict microstructure formation, where d_{cell} is the cell size; (b) a cross-sectional view of the network, where two growing grains are represented over the solid cells in blue.

where Q is the laser power, η_p is the fraction of the laser energy absorbed by the in-flight powder, r_b is the radius of the laser spot, and V_s is the laser scan speed. The fraction of the laser energy absorbed by the deposited part is denoted by η_l and evaluated by the Hagen-Rubens model as [23]:

$$\eta_l(T) = \sqrt{8\varepsilon_0 \omega R_e(T)} \tag{12}$$

Here ω is the angular frequency of the near-infrared laser, ε_0 is the permittivity, and $R_e(T)$ is the temperature-dependent resistivity. For IN718 alloy, $R_e(T)$ is empirically formulated as [24]

$$R_e(T) = \begin{cases} -0.96 + 0.005T - 3.919 \times 10^{-6}T^2 + 9.713 \times 10^{-10}T^3, & \text{for solid phase} \\ 1.251 + 1.364 \times 10^{-4}T, & \text{otherwise} \end{cases} \tag{13}$$

where T is given in units K and the resulting $R_e(T)$ has units Ω m.

Assuming that powder particles are spherical, the average temperature rise of the powder during the flight, ΔT, can be estimated as [19]

$$\Delta T = \frac{3\eta_m \eta_s Q\tau}{2\pi r_p r_b^2 c_p \rho_p} \tag{14}$$

where η_m is an interference factor to account for shielding of some particles from the laser beam by other particles, η_s is the fraction of laser power absorbed by the solid particles, r_p is the average radius of the powder particles, τ is the time of flight which depends on the velocity of particles and the length of flight, and c_p and ρ_p denote the specific heat and density of powder particles, respectively.

2.3. Numerical discretization

The heat transfer and fluid flow governing equations are solved using a finite volume method (FVM). In the implementation, the Pressure-Implicit with Splitting of Operators (PISO) scheme [25,26] is applied to the time integration. A structured mesh was used for the discretization of the region of interest for the DED process as shown in Fig. 1. For the numerical examples presented in Section 5, the size of the substrate is set to 22 mm × 8 mm × 5 mm, with 360 × 70 × 56 cells used to discretize it. The time step is set to 0.1 ms.

At the beginning of the simulation, all computational cells above the substrate are set to the properties of the inert gas (Argon); the initial temperature is set to ambient temperature 298 K. During the simulation, the thermo-physical properties of the inert gas cells located in the potential deposited part are assigned to those of the deposited material (e.g. IN718 alloy) according to the predefined raster pattern with the given laser scan speed. The initial temperature of the newly activated cells for the build part is set to ΔT given by Eq. (14) above the ambient temperature. When new metal cells are created, the boundary on which momentum and energy BCs are applied, namely, Eqs. (8), (10), (11), is updated.

3. Grain structure evolution model

The cellular automaton (CA) model [27,11] is applied to simulate the grain structure evolution, and extended to capture the common epitaxial growth mechanism seen frequently in AM processes. In the CA model, a set of cubic cells is used to discretize a material region as shown in Fig. 2. Each cell may have variables associated with it, such as temperature and a state index associating the cell with a particular grain. The grain structure evolution is governed by two sub-models, for nucleation and grain growth kinetics, which are introduced in the following sections.

3.1. Enriched nucleation model

The nucleation model used in CA determines the location of nucleation sites, activation criteria, and the crystal orientation of nucleated grains. In the original CA model for casting, nucleation can occur both at the surface of the mold and in the bulk of the liquid volume. However, there is no mold in the AM process, and an epitaxial growth phenomenon is often observed in experiments [28,3,5,29]. To accommodate these features using CA, an enriched nucleation model is used consisting of the bulk nucleations and activation of existing grains along the molten pool boundary.

3.1.1. Bulk nucleations

For bulk nucleations, number densities of sites are determined by a set of input parameters, such as the nucleation number density ϱ. These parameters are typically fitted to experimental measurements. Experimental data of 3D microstructures is difficult to obtain, so the

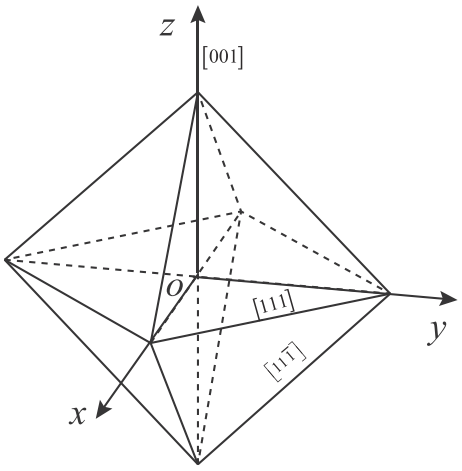

Fig. 3. Regular octahedron envelope.

nucleation number density was qualitatively estimated based on 2D experimental microstructures. Prior to the beginning of the simulation, the total number of nucleation sites in the bulk can be calculated as:

$$N_v = \varrho_v V \tag{15}$$

where the subscript v associates the variable with the bulk; V represents the total volume. For a given discretization, cells are randomly selected as potential nucleation sites: N_v cells from the set of all cells. Activation conditions, such as critical undercooling $\Delta T^{\text{critical}}$, of bulk nucleation sites are assumed to follow a Gaussian distribution characterized by parameters ΔT_{mean} and ΔT_σ, the mean and standard deviation of the distribution.

During the solidification process, a new grain is generated at a pre-chosen cell ν (while the cell is still entirely liquid) if the undercooling at the center of cell ν exceeds its assigned critical undercooling. Its crystallographic orientation is identified by a set of Euler angles (ψ_1, ψ_2, ψ_3), where $0 \le \psi_1 \le 2\pi$, $0 \le \psi_2 \le \pi$, and $0 \le \psi_3 \le 2\pi$, corresponding to the global orientation of its [001] crystal direction. Grains that are nucleated in the bulk of the volume are assumed to have random crystallographic orientations [30].

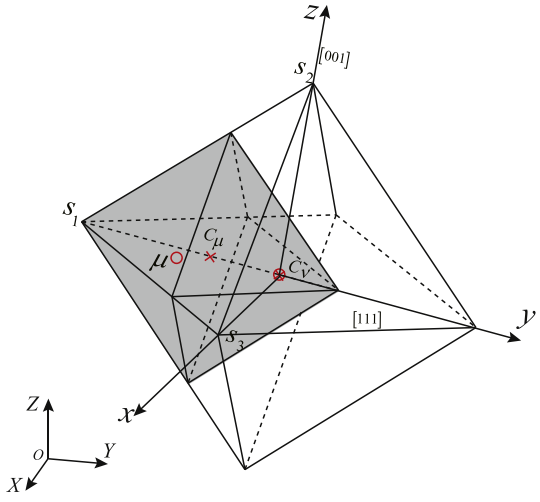

Fig. 4. The decentered octahedron algorithm: When the envelope associated with cell ν captures one of its neighboring cells, μ, a new envelope is placed in cell μ. The center coordinates and initial diagonal length of the new envelope are determined in a way such that one of its corners overlaps the closest corner of the original cell's envelope, where C_ν and C_μ (indicated by the cross) are the centers of the envelopes of cell ν and μ, respectively. Centers of the cells are marked by the red circle.

3.1.2. Activation of existing grains along the molten pool boundary

In AM, when the material of the substrate is the same as that of the powder particles and the liquid wets the substrate completely, an epitaxial grain growth phenomenon is often observed. Existing grains from the substrate or the partially melted metal powder at the molten pool boundary act as seed crystals and continue to grow. To numerically model this phenomenon, we propose the following model to activate the existing grains along the molten pool boundary without resolving the micro-scale details of the mechanism [31]. First, the initial grain structures of the substrate and metal powders are assumed to be equiaxed, as is common in the physical process. During each single track scan, the corresponding grain structures of the material within the molten pool disappear as the material melts; the corresponding cells become liquid. The existing grains within the mushy zone surrounding the entire boundary of the molten pool are then activated to grow based on epitaxial growth model described in Appendix A, and we assume that they keep their inherent crystallographic orientation.

3.2. Grain growth model

In the CA model, the dendritic structure details are not resolved but modeled by a combination of envelopes; an envelope is defined as a "smooth surface" surrounding all dendrite tips of a grain. For cubic crystals, e.g. face-centered cubic (FCC), the preferred dendritic growth direction is ⟨100⟩. Therefore, the corresponding envelope has an octahedral shape bounded by {111} faces as shown in Fig. 3; the six half-diagonals of the octahedral envelope represent the ⟨100⟩ crystallographic directions defined by the Euler angles, along which the grain grows fastest.

A polynomial function to relate the grain growth with the local undercooling is implemented for computational efficiency. Based on the Lipton-Glicksman-Kurz (LGK) model [32], the dendrite tip growth rate, v, is a function of the undercooling, $\Delta T = T_l - T$, where T_l is the liquidus temperature. Because the LGK model is nonlinear and will be computationally expensive if implemented, such a

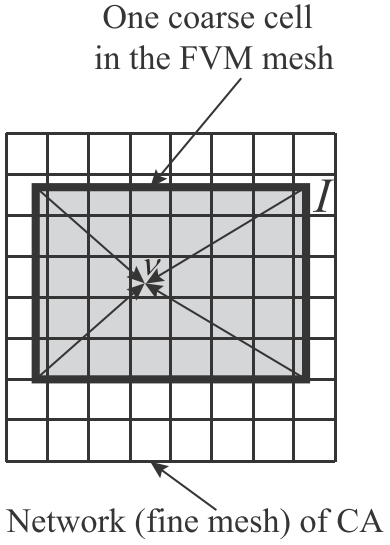

Fig. 5. Schematic illustration of the estimation method for a 2D case. The temperature at the center of CA cell ν is interpolated from a rectangular cell in the FVM mesh.

Table 1
Thermo-physical properties of the substrate and IN718 alloy powder.

Property	IN 718	Reference
Solid density ρ_s ($kg\,m^{-3}$)	7734	[39]
Liquid density ρ_l ($kg\,m^{-3}$)	7578	[39]
Solidus temperature T_s (K)	1533	[39]
Liquids temperature T_l (K)	1609	[39]
Solid specific heat c_{ps} ($J\,kg^{-1}\,K^{-1}$)	435	[39]
Liquid specific heat c_{pl} ($J\,kg^{-1}\,K^{-1}$)	775	[39]
Solid thermal conductivity k_s ($W\,m^{-1}\,K^{-1}$)	11.4	[40]
Liquid thermal conductivity k_l ($W\,m^{-1}\,K^{-1}$)	31.3	[40]
Latent heat of fusion L ($kJ\,kg^{-1}$)	290	[39]
Dynamic viscosity μ ($Pa\,s$)	5.31×10^{-3}	[41]
Temperature coefficient of surface tension $\frac{d\sigma}{dT}$ ($N\,m^{-1}\,K^{-1}$)	2.5×10^{-5}	[42]
Expansion coefficient β ($m\,K^{-1}$)	1.3×10^{-5}	[39]

Table 2
Parameters for the heat source model.

Parameter	Value	Reference
Absorption fraction by the in-flight powder η_{lp}	0.3	[20]
Absorption for solid η_s	0.3	[19]
Interference factor η_{lm}	1.0	[19]
Convective heat transfer coefficient h_c ($W\,m^{-2}\,K^{-1}$)	100	[20]
Emissivity ϵ	0.3	[20]
Angular frequency of the laser ω ($rad\,s^{-1}$)	1.75×10^{15}	[23]
Permittivity ε_0 ($F\,m^{-1}$)	8.85×10^{-12}	[23]
Reference temperature T_{ref} (K)	298	–
Stefan-Boltzmann constant $\hat{\sigma}$ ($W\,m^{-2}\,K^{-4}$)	5.67×10^{-8}	[23]

Table 3
Nucleation site parameters used in example simulations.

$\Delta T_{v,\mathrm{mean}}$ (°C)	$\Delta T_{v,\sigma}$ (°C)	ϱ_v (mm^{-3})
9.5	2.0	1.0×10^6

relationship is fitted with a polynomial approximation in this work as follows:

$$v(\Delta T) = \lambda_1 \cdot \Delta T + \lambda_2 \cdot \Delta T^2 + \lambda_3 \cdot \Delta T^3 \tag{16}$$

where λ_1, λ_2, and λ_3 are fitting coefficients and their values are determined as detailed in Appendix B. Aside from the LGK model, the KGT model [33,34], extended KGT model [35,14], and phase field simulations [36] have been used to build the relationship between the dendrite tip growth rate and the local undercooling; reasonable grain structure results were also obtained for AM [34,14], which indicates that the grain structure may not be very sensitive to the growth model. However, a quantitative comparison to elaborate the effect of these growth models on the resulting grain structure is an interesting topic, which is outside of the scope of this study.

The grain growth is represented by the growth of envelopes driven by the undercooling at the centers of cells. For a grain nucleating from an activated nucleation site, e.g. cell ν, a regular octahedral envelope is placed in the cell. The envelope center coincides with the center of the cell itself. Ignoring the incubation time, the lengths of the six half-diagonals at time t are obtained by

$$l_\nu(t) = \int_{t_\nu}^{t} v\left(\Delta T_\nu(\tau)\right) \mathrm{d}\tau \tag{17}$$

where t_ν represents the time at which the grain is nucleated. At some point, the octahedral envelope may "capture" a neighboring cell, e.g. cell μ, by engulfing the center of the cell. At this point, the growth process is re-initialized in cell μ by creating a new regular octahedral envelope that inherits the grain orientation from its counterpart in cell ν. The undercooling at the center of cell μ is then used to drive the growth of the new envelope. As a consequence, the cells that make up the grain each have their own octahedral envelopes. Although each of these envelopes grows uniformly based on the local undercooling of the owning cell, the growth velocity of the grain is a function of the local temperature throughout the grain, and can be non-uniform in space and time. Thus the growth of a grain is anisotropic. A grain envelope stops growing and is "deactivated" when all of the cells neighboring its owing cells have been captured. In this work, neighbors are defined as all cells that share a face, edge, or corner, so that a typical interior cell in 3D has 26 neighbors. In addition, a decentered octahedron growth algorithm, as schematically illustrated in Fig. 4, is used to determine a new octahedral envelope for the captured cell μ. This is done to ensure that the final grain orientation is not biased by the grid orientation. Details of the implementation of this method are given by Lian et al. [30].

4. Coupling of cellular automaton and finite volume methods

A one-way coupling method is used to couple the cellular automaton model presented in Section 3 to the heat transfer and thermocapillary flow model in Section 2.

Because the two models resolve different physics, requiring different computational resolutions, two sets of mesh cells are used in CA and FVM, respectively. The mesh used in the FVM is coarser than that in CA, and temperature data solved by the coarser mesh is transferred to the finer mesh. At each time step for CA simulation, the CA cell's temperature is interpolated from the coarse cell that covers the center of it. Because the time step used in FVM is larger than that in CA, a linear interpolation is used to compute the nodal temperature, T_I^t, of FVM cell at time t between two adjacent time step results, e.g. t^{n-1} and t^n, where superscript n denotes the nth time step in the FVM simulation:

$$T_I^t = \frac{T_I^n - T_I^{n-1}}{t^n - t^{n-1}}(t - t^{n-1}) + T_I^{n-1} \tag{18}$$

where $t^{n-1} \le t < t^n$. Then, as shown in Fig. 5, the temperature at the center of CA cell, e.g. $\boldsymbol{C}_\nu$, is obtained based on estimation scheme as follows.

$$T_\nu^t = N_I(\nu) T_I^t \tag{19}$$

where $N_I(\nu)$ is the estimation function associated with the node I of FVM cell that covers the CA cell ν. For example, N_I may be taken to be the first-order finite element shape functions [37] defined on the cell.

5. Results and discussions

Two sets of numerical examples were conducted in order to study the effects on microstructure of the various process parameters, including the laser power, laser scan speed, and raster pattern. In the first set, a series of single track simulations was carried out while

Table 4
Growth kinetics for IN718 alloy.

$\lambda_1 = 1.77 \times 10^{-5}\ m/(s \cdot K^{-1})$	$\lambda_2 = 1.58 \times 10^{-5}\ m/(s \cdot K^{-2})$	$\lambda_3 = 2.29 \times 10^{-6}\ m/(s \cdot K^{-3})$

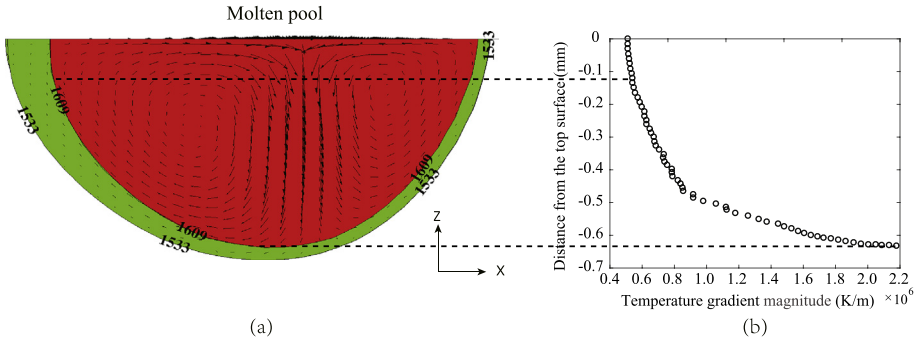

Fig. 6. Molten pool and thermal characteristic at time $t = 3$ s (a) *XZ*-plane section of the molten pool with surrounding mushy zone; arrows indicate the flow field, which is dominated by the Marangoni effect [43]. Dashed lines between sub-figures link the profile points to their coordinates in the right sub-figure. (b) Temperature gradient magnitude profile along the boundary of the molten pool within the *XZ*-plane section.

varying the first two parameters (laser power and scan speed). In the second set, thin vertical wall builds with different raster patterns were modeled, in accordance with the experiments by Parimi et al. [5].

Parameter values for all simulations are summarized in Tables 1 and 2 for the thermocapillary flow model, and in Tables 3 and 4 for the CA model. Moreover, the initial grain structure for the substrate is numerically generated to give equiaxed grains with random crystal orientations to replicate the rolled IN718 sheet with uniform fine grain used in the experiment [5] for the DED IN718 alloy, with an initial average grain size is 15.7 μ m (equivalent sphere diameter). It has been proved that aspects of the CA result are sensitive to the cell spacing, i.e., a finer mesh leads to a larger number of small grains; however, similar patterns for the larger grains will be obtained as the cell spacing is decreased [30]. In all the simulations below for the modeling of grain structure, a cell size of $d_{\text{cell}} = 2.5$ μ m was chosen to balance resolution and the computational efficiency. All grain morphology and crystallographic analysis were conducted using the software Dream3D [38].

5.1. Results of single scan track

The grain structure in AM under different laser powers and scan speeds for single-pass builds can reveal important findings about the

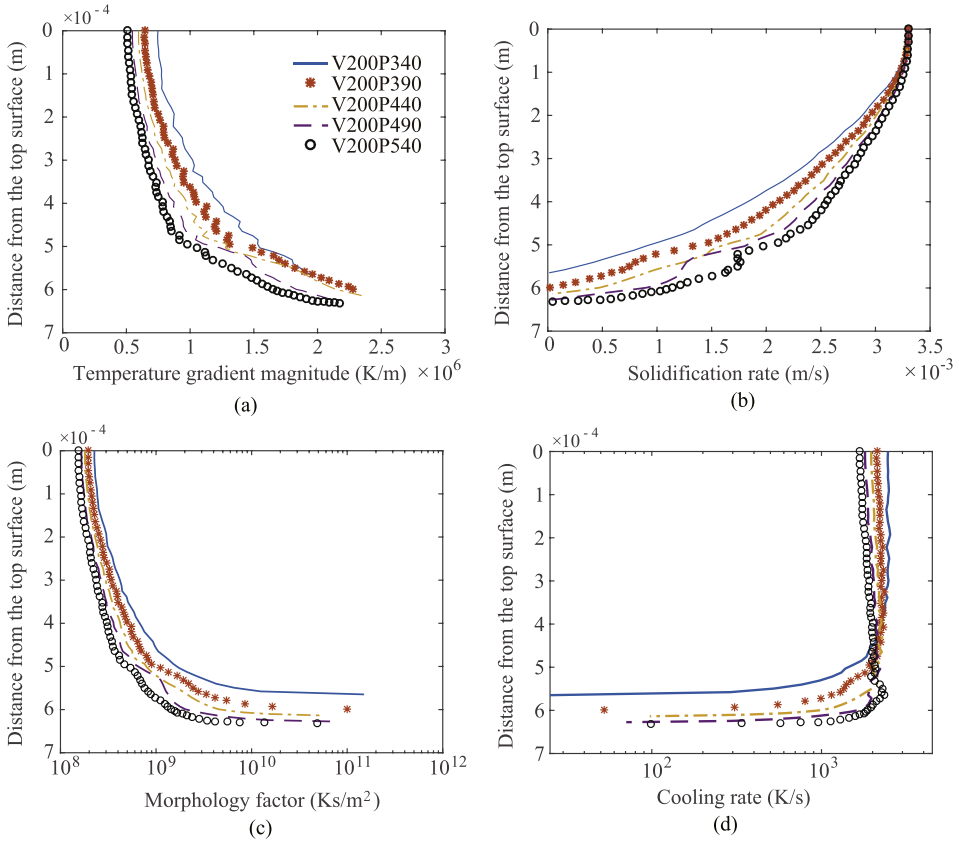

Fig. 7. Thermal profiles along the boundary of the molten pool within the *XZ*-plane section at time $t = 3$ s: (a) temperature gradient magnitude *G*, (b) solidification rate *V*, (c) morphology factor $M = G/V$, and (d) cooling rate $C = G \cdot V$, for cases with laser power varied within the range [340 W, 540 W], and constant laser scan speed of 200 mm/min. All profiles are aligned to the top surface of the molten pool; the abscissa represents the molten pool depth.

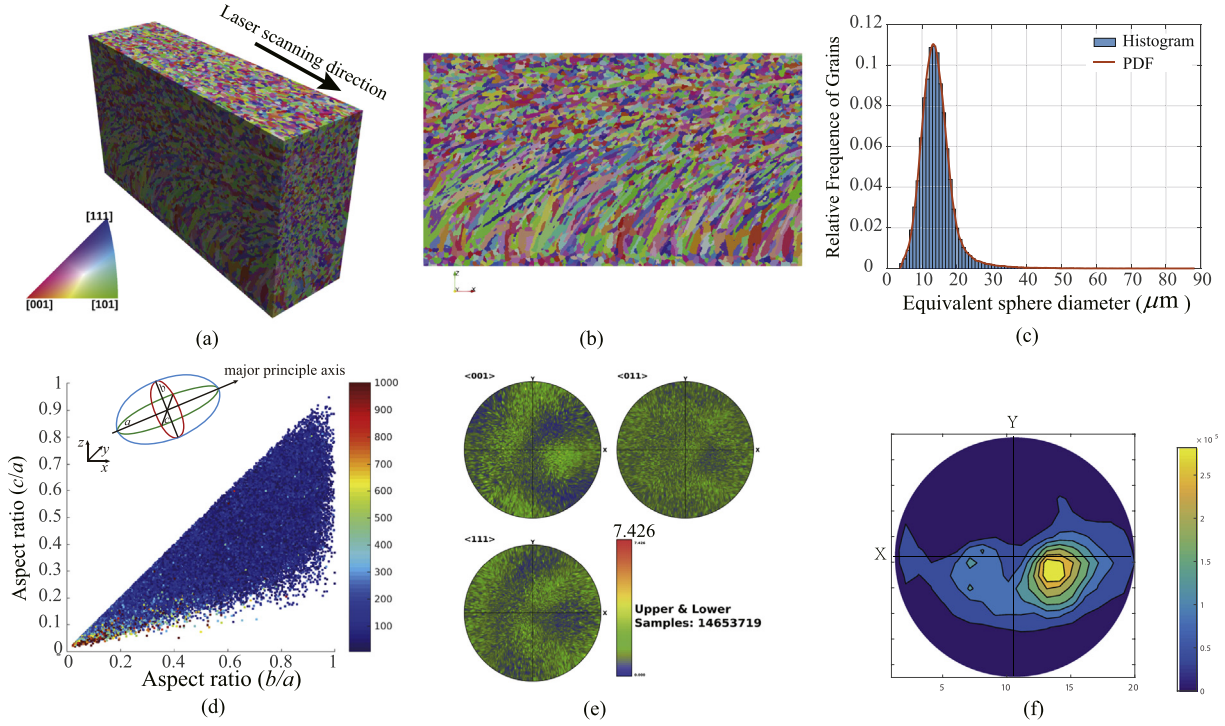

Fig. 8. Simulation results of the case with laser power of 540 W and scan speed 20 mm/min: (a) 3D view of the grain structure; (b) *XZ* cross-sectional view of the grain structure; (c) histogram of the grain size distribution; (d) aspect ratio of the grains, where the color corresponds to the grain size as measured by the total number cells it occupied; (e) pole figure of the grain structure; (f) grain shape orientations distribution.

microstructure evolution. In this set of simulations, the computational model is as described in Section 2.1. Only one 0.35 mm-thick deposited layer with length of 20 mm was simulated here. The region size of interest for CA is set to 1.2 mm × 0.35 mm × 0.675 mm (x, y, z). The CA region is taken 9.2 mm from the edge along the x axis.

5.1.1. Example case

A first case with laser power of 540 W and scan speed of 200 mm/min is presented here in detail. Hereafter, we label this case V200P540, where "V" indicates the laser scan speed and "P" the laser power. The thermal characteristics surrounding the molten pool boundary along with the flow field are presented to elucidate the underlying physics for the as-built grain structure formation. The molten pool is defined as any location where the temperature is above the liquidus temperature, while the mushy zone is defined as any location where the temperature is between the liquidus and solidus temperatures. A snapshot of a longitudinal cross-section (*XZ* plane) view is shown for representative time $t = 3$ s in Fig. 6 (a),

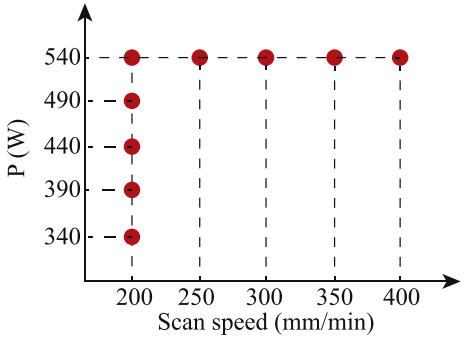

Fig. 9. Design of the single track case study; each solid dot stands for a case with the combination of the laser power and scan speed.

where the molten pool is in red and the surrounding mushy zone in green; arrows denote velocity vectors of the thermocapillary flow inside the molten pool. The region of interest is the mushy temperature region for the CA simulation, because this is where the critical undercooling is achieved first due to thermal conduction into the deposited material and substrate. In Fig. 6 (b), a profile of the magnitude of temperature gradient G is plotted along the liquidus isotherm in the *XZ* plane. The profiles of solidification rate V_{sr}, morphology factor $M = G/V_{sr}$ and cooling rate $C = G \cdot V_{sr}$ at the same locations and time are provided in Fig. 7. These factors are commonly used to study solidification patterns and grain sizes since they can reveal important trends [44]. From Fig. 7 (a) and (b), the smallest G and the largest V_{sr} are found at the surface of the molten pool (namely the tail of the molten pool), while the largest G and the smallest V_{sr} at the bottom of molten pool. Meanwhile, the morphology factor M and the cooling rate C shown in Fig. 7 (c) and (d) follow the trends of G and V_{sr}, respectively.

The thermal characteristics presented above influence the resulting grain structure. Based on the qualitative conclusions of Hunt's model [45] regarding G and V_{sr}, it is expected that the equiaxed grains tend to appear at the tail of the molten pool and columnar grains dominate at the bottom. These phenomena are apparent in Fig. 8, where the 3D view and the *XZ* plane of symmetry of the resulting grain structure are presented in (a) and (b), respectively. Lattice orientations are denoted by an inverse pole figure (IPF) map with a color key as shown in Fig. 8 (a). The columnar grains grow upward epitaxially from the molten pool bottom until they impinge on the grains from bulk nucleations occurring ahead of them; the location of this columnar-to-equiaxed transition (CET) depends on multiple factors [18], e.g. nucleation model parameters, grain growth kinetics, and thermal conditions; this dependence is a complex problem and will be studied further in the future.

Additional grain statistics are provided in Fig. 8 (c) –(f). In Fig. 8 (c), a histogram of grain size distribution is plotted and demonstrates

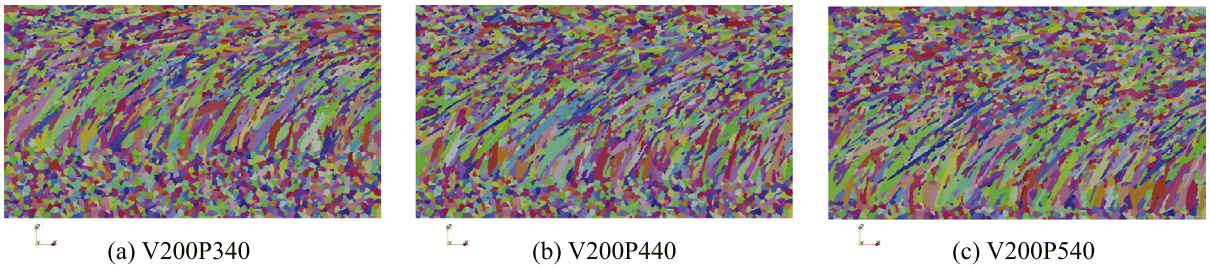

Fig. 10. XZ cross-sectional view of grain structure for cases with laser scan speed of 200 mm/min and the power of (a) 340 W, (b), 440 W and (c) 540 W.

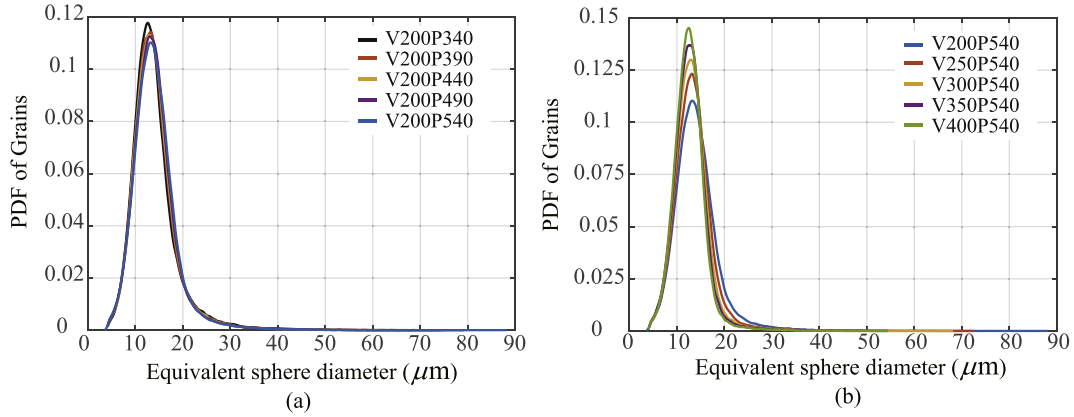

Fig. 11. Probability distribution function of grain size quantified by equivalent sphere diameter: (a) Constant laser scan speed (200 mm/min), variable laser power value within the range of [340 W,540 W]; (b) Constant laser power (540 W), variable scan speed within the range of [200,400] mm/min.

that most of the grains have size less than 20 μ m, as characterized by equivalent sphere diameter; meanwhile, the probability density function (PDF) curve in red is extracted from the histogram. To characterize grain shapes, an ellipsoid is used to fit each grain with $a \geq b \geq c$ as the principle semi-axes. The combination of aspect ratios, b/a and c/a, serves as a geometric indicator for an equiaxed shape if $a \approx b \approx c$, a columnar shape if $b/a \ll 1$ and $c/a \ll 1$, or a disk if $a \approx b \gg c$. In Fig. 8 (d), the aspect ratios (b/a and c/a) are plotted, with each dot representing a grain and color indicating the grain size in units of CA grid cell volumes. It is evident that the finest grains are equiaxed grains as their aspect ratios are close to the upper right corner; the coarser grains are columnar grains occupying the lower left corner of Fig. 8 (d). In Fig. 8 (e), the ⟨001⟩ pole figure, the preferred orientation of many grains is best aligned to the temperature gradient, as ⟨001⟩ is the crystallographically favored growth direction for face-centered-cubic (FCC) alloys. In addition, the grain shape orientation distribution representing the direction of the major ellipsoid axis is plotted in Fig. 8 (f). It is found that there is one preferred shape orientation located in the $+x$ region but close to the x-axis, indicating that the major axis of most grains tilts in the laser scan direction to follow the temperature gradient. Thus, the temperature gradient dictates not only the crystal lattice orientation as shown by Fig. 8 (e) but also the grain shape orientation as shown in Fig. 8 (f).

5.1.2. Laser power effect on grain structure

To clearly illustrate the relationship between laser power and resulting grain structure, we designed simulation cases with constant scan speed of 200 mm/min and laser power varying from 340 W to 540 W as shown in Fig. 9 for clarity. The selected process parameters are in the range of experimental conditions for DED in reference [5]. Energy density in these cases is neither so high that a

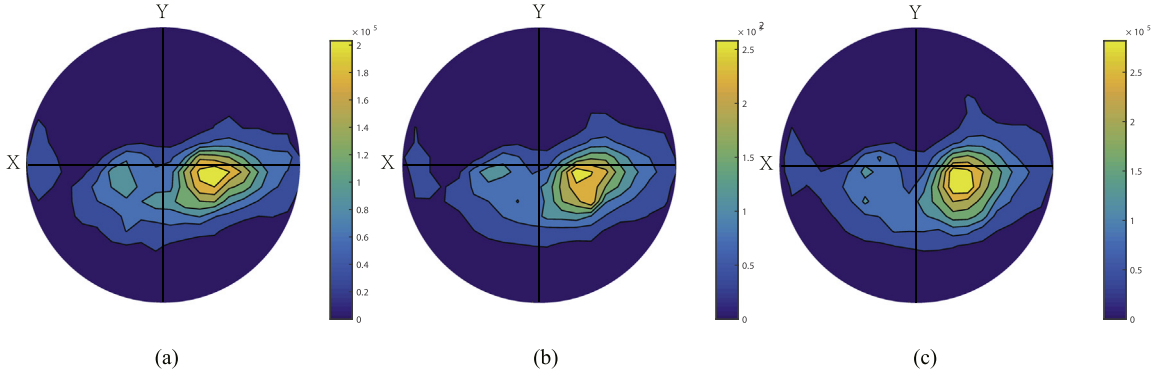

Fig. 12. Grain shape orientation distributions for scan speed 200 mm/min and variable laser power: (a) 340 W, (b) 440 W, and (c) 540 W.

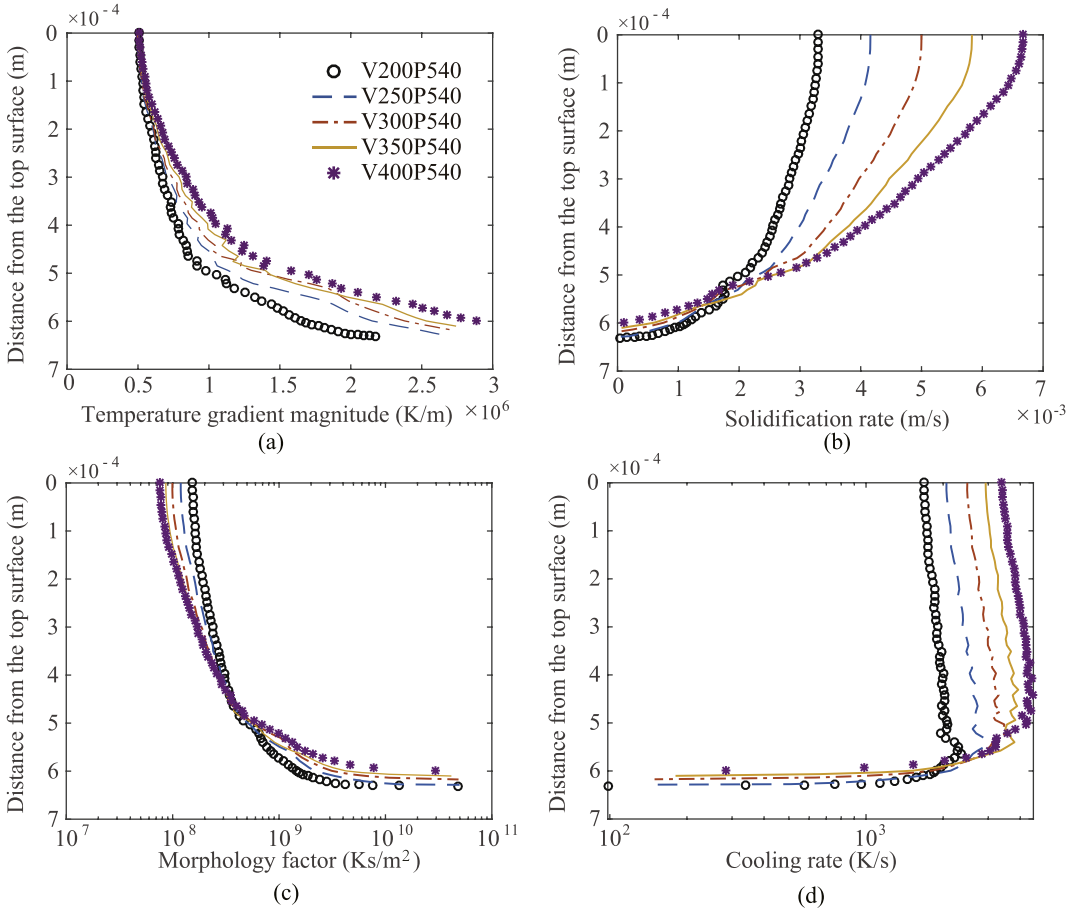

Fig. 13. Thermal profiles along the boundary of the molten pool within the *XZ*-plane section at time $t = 3$ s: (a) temperature gradient magnitude G, (b) solidification rate V_{sr}, (c) morphology factor $M = G/V$, and (d) cooling rate $C = G \cdot V$, for cases with laser scan speed varied within the range [200, 400] mm/min, and constant laser power of 540 W. All profiles are aligned to the top surface of the molten pool; the abscissa represents the molten pool depth.

keyhole is formed during the process, nor so low as to result in lack of fusion.

First, the thermal profiles under the varied laser power are introduced. For these cases, the temperature gradient magnitude, solidification rate, morphology factor and cooling rate profiles are plotted in Fig. 7 (a), (b), (c), and (d), respectively. In Fig. 7 (a), the magnitude of temperature gradient profiles show the same trend (namely, its value increase from the top surface to the bottom of the molten pool) with a slight shift among cases. In Fig. 7 (b), the solidification rate curves are similar among cases. Fig. 7 (c) shows that the morphology factor profiles follow the trend shown in Fig. 7 (a); Fig. 7 (d) indicates that cooling rate decreases with laser power in most of the molten pool domain.

The effects are identified from the comparisons of grain morphology, grain size distribution, and the grain shape orientation distribution. Take the cases of 340 W, 440 W, and 540 W as examples (variations among all cases are similar). As shown in Fig. 10 for the cross-sectional view of the grain structure, a CET appears in all the cases and there is no significant difference among them, which is in accordance to the morphology factor profiles presented in Fig. 7 (c). The PDF curves for grain size distribution are presented in Fig. 11 (a). It is shown that the grain size becomes relatively coarser with the increase of the laser power, i.e., the peak of the curves moves to upper left. This variation corresponds to the cooling rate profile changes in Fig. 7 (c), indicating that the smaller the cooling rate, the coarser the grain size. Fig. 12 presents grain shape orientation distributions. From the comparison, similar contours are obtained but with a difference in the isolines and their distributions among the three cases. The laser power is seen to have at most a weak influence on the shape orientation of the grains.

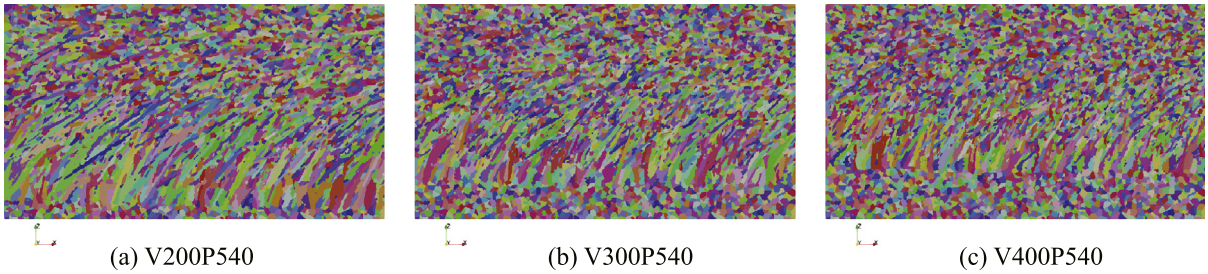

Fig. 14. *XZ* cross-section of the grain structure for cases with constant laser power of 540 W and scan speed of (a) 200, (b) 300, and (c) 400 mm/min.

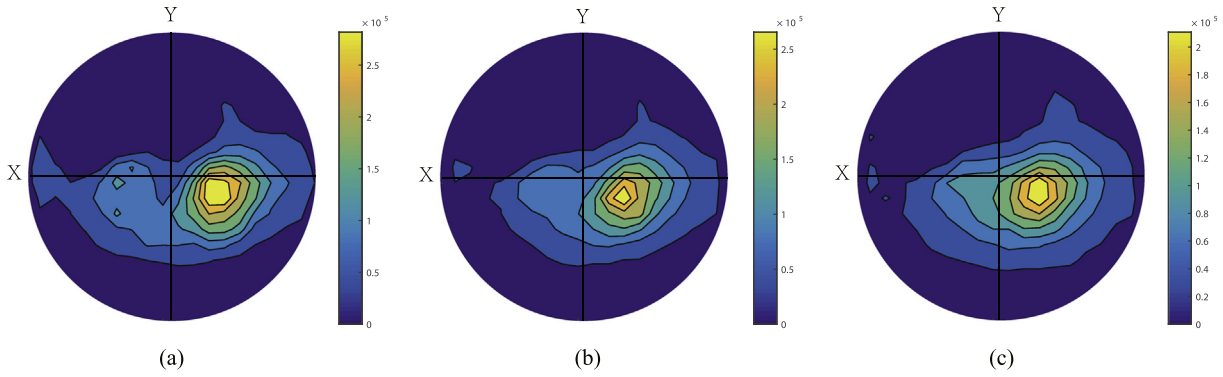

Fig. 15. Grain shape orientation distributions for cases with constant laser power of 540 W and scan speed of (a) 200, (b) 300, and (c) 400 mm/min.

5.1.3. Laser scan speed effect on grain structure

To study the influence of the laser scan speed on the grain structure, four other additional cases are conducted with a constant laser power (540 W) and laser scan speeds of 250, 300, 350, and 400 mm /min as listed in Fig. 9. Fig. 13 (a) –(d) displays the same four thermal profiles plotted in Fig. 7 (a) –(d). In Fig. 13 (a), the magnitude of temperature gradient profiles shows small variation among cases at the region close to the top of the molten surface, while at the bottom of the molten pool the temperature gradient increases with the scan speed. In Fig. 13 (b), the solidification rate increases with the laser scan speed in most of the molten pool. Fig. 13 (c) shows a slight increase in the morphology factor with scan speed in the top region, but the opposite trend at the bottom. The cooling rate profiles in Fig. 13 (d) show the same trend as the solidification rate, and clearly demonstrate a strong relationship between these quantities and the scan speed for a given laser power. In addition, the molten pool depth decreases as the laser scan speed increases because of the lower energy density input. It is clear the effect of laser scan speed is more significant particularly on morphology factor and cooling rate than that of laser power in this study.

Since the variations among the five cases are similar, only the 200, 300 and 400 mm/min scan speed cases are shown for comparison. Fig. 14 shows the *XZ* cross-sections of grain structures of the three cases. One can see that the size of the coarse grains becomes smaller with an increase in scan speed, which is related to morphology factor profiles in Fig. 13 (c). This effect can also be seen in the grain size distribution plot in Fig. 11 (b) corresponding to cooling rate profiles in Fig. 13 (d). Moreover, the grain shape orientation distributions for these cases are plotted in Fig. 15, demonstrating the influence of the laser scan speed on the tilt angle of the grains through changing the temperature gradient directions.

5.2. Raster pattern effect on grain structure

Multiple-layer simulations with different raster patterns were conducted following as closely as possible the experimental set-up of Parimi et al. [5]. Each layer in these builds is a single scan track, with an average layer thickness reported as 0.35 mm. Other setting parameters are summarized in Table 5. Two build cases with unidirectional (denoted by B1) and bi-directional (B2) scans, respectively, are presented below.

In these multiple-layer builds, heat accumulates over multiple laser passes. It is important to capture this phenomenon as it affects the molten pool depth and thermal characteristics such as G, V_{sr}, M, and C. In Fig. 16, these temperature characteristics are plotted for each of the first 8 layers for the unidirectional build case; all values are plotted at a time 3 s into the deposition of the given layer. It is shown that variations exist among these profiles but become smaller with the addition of more layers. In addition, the trends of each profile along the molten pool depth share the same features detailed in Section 5.1.1. Therefore, the size of region of interest for CA is set to 0.6 mm × 0.35 mm × 3.05 mm (x, y, z), which consists of a part of the substrate and the first 8 build layers of the part as illustrated by the white outline in Fig. 17. The thermocapillary flow simulation domain for the build part was 20 mm × 8 mm × 8.5 mm (x, y, z), while the region of interest for grain structure was taken 10.5 mm from the side of the thermal domain along x-axis.

Simulated grain structures are presented in Fig. 18, and the corresponding electron backscatter diffraction (EBSD) images of experimental results are shown in Fig. 19. Considering that the grain structure statistics of the experiments are not provided in [5] and some simulation parameters, e.g. nucleation density, are assumed in this work, a direct quantitative comparison of grain structure statistics between the 2D experimental results and the 3D simulated results is not presented here. Therefore, we conducted only a qualitative comparison between the EBSD images and the simulated *XZ* cross-sections of the grain structure at the center of the build parts to show the raster pattern effect on grain structure. As plotted in Fig. 18 (a) for Cases B1, the *XZ* cross-sections of the grain structure demonstrate that the columnar grains are unidirectionally oriented at an angle of around 60° to the substrate in all layers, which is close to the experimental results with the oriented angle of 50°–60° [5]. The similar trends show that the inclination follows the rear of the melt pool in each layer. Additionally, the "sandwich structure "(i.e., the columnar and equiaxed grains appearing alternately) in the experiments is reproduced in the simulated results. Although the size of the fine-grain region formed at the inter-layer interface of simulated grains is clearly larger than that of the experimental results, it decreases from the bottom upwards, following the same trend as in the experimental results. For case B2, because of the bi-directional scans, the columnar grains are oriented in a "zig-zag" pattern tracking the rear of the melt pool in each layer, which can be also found in the experimental result (Fig. 19 b). Although the fine-grain zone of B2 is not as prominent as in B1 in the experiments, Fig. 19 (b) also shows the "sandwich structure" that was produced in the simulation result as shown in Fig. 18 (d). From the comparison, it is evident that a qualitative agreement regarding grain structure between simulation and experimental results is achieved.

Table 5
Processing parameters, taken from experiments in [5].

	Build 1 (B1)	Build 2 (B2)
Raster pattern	Unidirectional	Bi-directional
Laser power P (W)	390	390
Scan speed V_s(mm/min)	200	200
Laser operation	6 s pause between scans	Continuous
Laser beam radius r_b (mm)	0.35	0.35
Flight time τ (s)	2.5×10^{-3}	2.5×10^{-3}

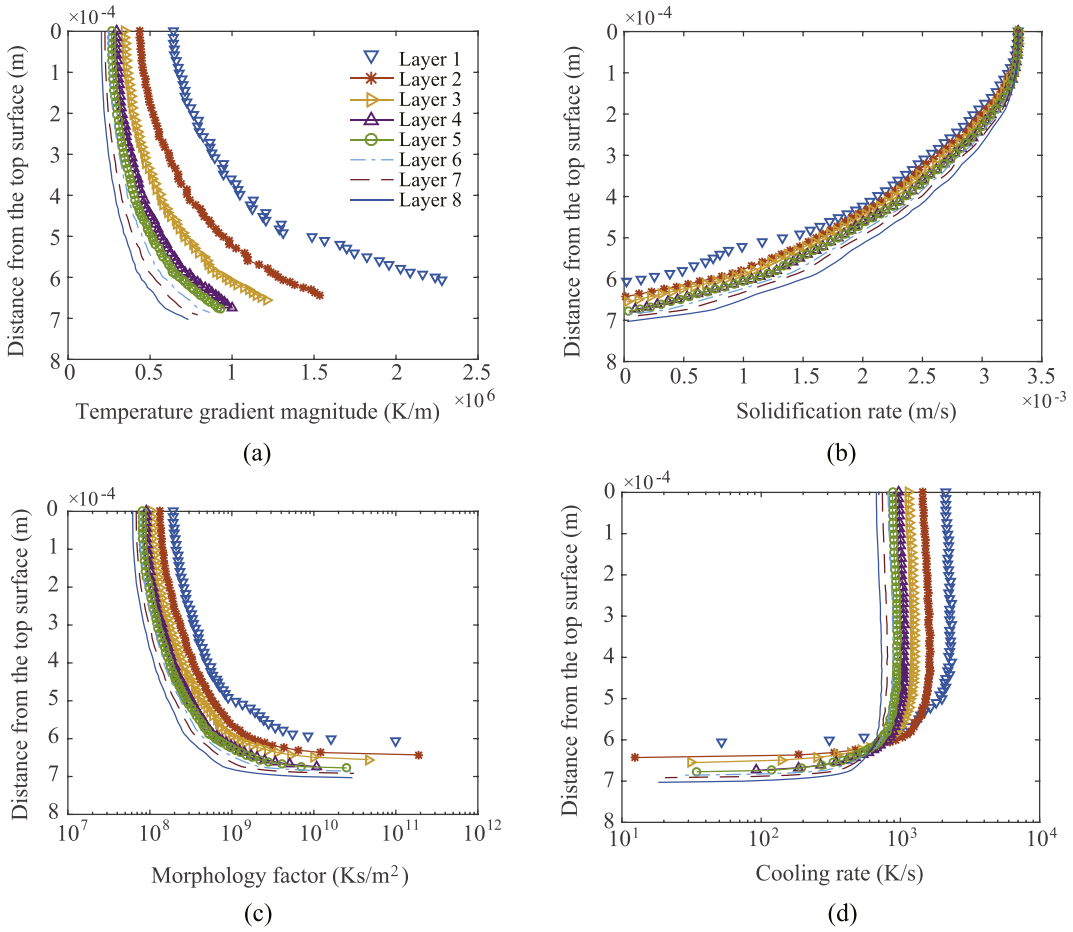

Fig. 16. Thermal profiles along the boundary of the molten pool within the *XZ*-plane section for the first 8 layers at time $t = 3$ s from the beginning of each track: (a) temperature gradient magnitude G, (b) solidification rate V_{sr}, (c) morphology factor $M = G/V$, and (d) cooling rate $C = G \cdot V$. All profiles are aligned with the top surface of the molten pool; the vertical axis represents the molten pool depth.

The 3D views of the as-built grain structures from the simulations are shown in the second column of Fig. 18 as well as the pole figures of grain orientations in the third column. From the pole figures, the random degrees of B1 and B2 cases are 4.091 and 3.214, respectively, indicating a weak texture in both cases, with some points in red located along the $+x$ axis for the B1 case and along the $+x$ and $-x$ axes for the B2 case, indicating that some preferred orientations exist following the direction of the thermal gradient caused by the moving laser.

In addition to the IPF and PF figures above, the 3D grains statistics are studied. Fig. 20 is the histogram of grain size distributions;

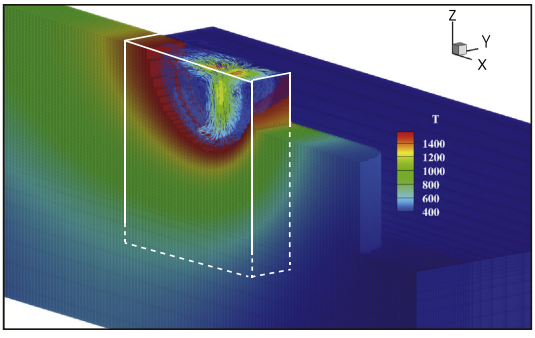

Fig. 17. Temperature field of the build and thermocapillary flow inside the molten pool; white solid/dashed lines outline the CA region in the *X*, *Y*, and *Z* directions.

the curves for the two cases almost fully overlap each other. The aspect ratios (b/a and c/a) of the best-fit ellipsoids are plotted in Fig. 21, where each dot represents a grain and is colored by grain size as quantified by the total number of CA cells. It is qualitatively demonstrated that the largest grains are columnar grains, mainly distributed near the lower left corner of the figure. The orientation distribution of largest principle axis of each grain is shown in Fig. 22, where the legend indicates the total number of grains. It can be seen that there is one preferred orientation for the grains in Case B1, and two for the grains in Case B2, representing the alternating orientations in adjacent layers.

These simulation results show qualitative agreement with experiments, and shed light on the evolution of the grain structure. In the deposition of each layer, the mechanisms of formation of coarse and fine grains are similar to those explored in Section 5.1. The sandwich structure arises because as each layer is deposited, a columnar-to-equiaxed transition forms because of the competition between epitaxially growing columnar grains and bulk-nucleated equiaxed grains. When a new layer is added, some of these equiaxed grains are partially remelted and grow epitaxially, forming an alternating structure. The raster pattern plays an important role in controlling not only the crystal orientation distribution as shown in Fig. 18 (c) and (f), but also the grain shape orientation distributions as shown in Fig. 22. Therefore, the unidirectional scan pattern leads to the unidirectional inclination of the grain pattern in Case B1, and the bi-directional scan pattern to the “zig-zag” grain pattern in Case B2. Aside from the two raster patterns studied here, there are

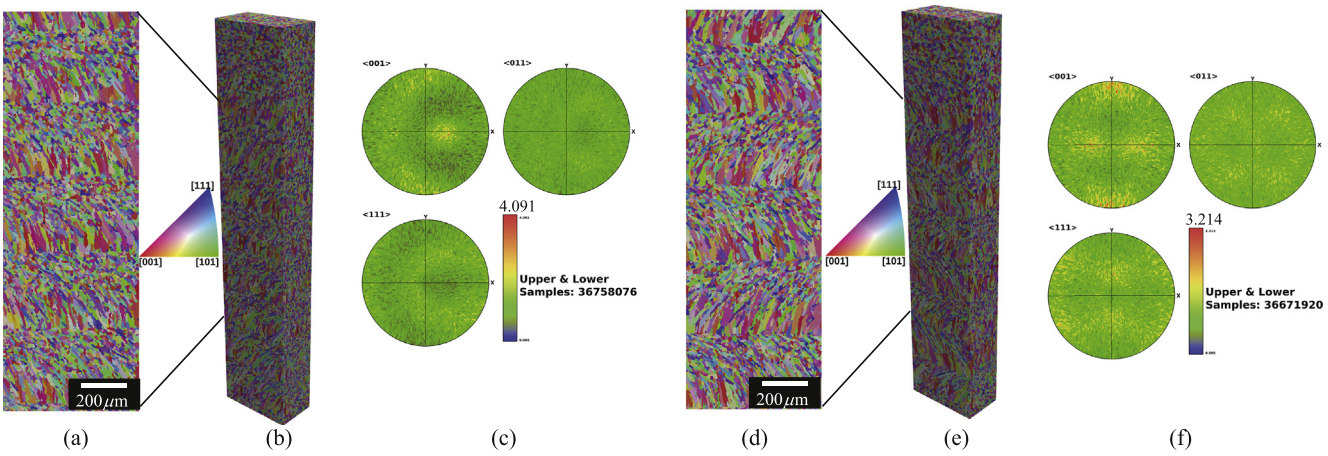

Fig. 18. Microstructure simulation results for multi-layer AM builds. The first row corresponds to the Case B1 with a unidirectional raster pattern; the bottom row to the Case B2 with a bi-directional raster pattern. (a) and (d): *XZ* cross section view of simulation results; (b) and (e): 3D views of simulation results; (c) and (f): pole figures (PF) of 3D simulation result. Color in (a)–(b), (d)–(e) corresponds to grain orientation as shown in the inverse pole figure (IPF) triangle legend.

many other complex patterns, such as meander, stripe, and chessboard patterns as shown in Fig. 23. Although these patterns are not addressed here, the resulting grain structure can be predicted based on the grain features obtained in the unidirectional and bi-directional scan patterns and considering the hatching space. Taking the meander pattern as an example, in the build direction the feature

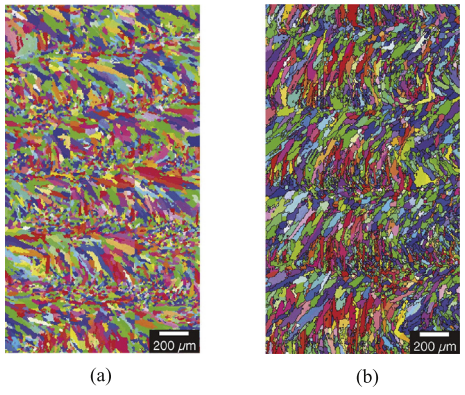

Fig. 19. EBSD images of the cross sections adopted from the work of Parimi et al. [5]:(a) Case B1, (b) Case B2.

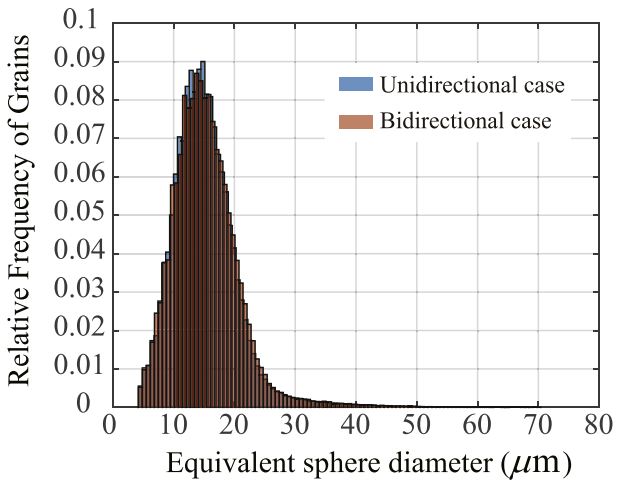

Fig. 20. Comparison of simulated grain size distribution for the B1 and B2 cases.

of the grain structure is expected to be similar to that of the unidirectional pattern for the thin wall, but the inclination of the grains will be a function of *x* and *y* due to the multi-scans in the *XY* plane. The detailed grain structure caused by these patterns will be studied in our future work.

6. Conclusion

The grain structure and morphology in the directed energy deposition (DED) of the IN718 alloy have been studied numerically using a proposed 3D cellular automaton finite volume method. It is demonstrated that the proposed model can predict the mixture of fine and coarse grains under the complex 3D transient thermal conditions in the DED process. Based on the present study, it is demonstrated that:

1. The grain structure size becomes finer as laser scan speed increases or laser power decreases;
2. Compared with laser power, laser scan speed has a stronger effect on the morphology factor profiles as well as cooling rate and the resulting grain structure;
3. Crystal orientation and the major principal axis of the columnar grains distributions inside the molten pool follow the direction of temperature gradient in the mushy zone; and
4. The raster pattern plays an important role in determining the grain structure throughout the part as it influences the temperature gradient direction during the solidification.

Our goal was to establish a relationship between process parameters and the grain structure formed for additive manufacturing process. The findings in this paper can inform ways to choose process parameters for better microstructural control towards more widely used load-bearing DED parts. Future work will include other microstructure-governing physics such as grain coarsening and solid state phase transformations. Understanding the latter is important because secondary phases can have large effects on material performance. The coupling of CA with kinetic Monte Carlo and phase field to incorporate the coarsening and phase change phenomena is one possible way to explore these phenomena.

Data availability

The raw/processed data required to reproduce these findings cannot be shared at this time as the data also forms part of an ongoing study.

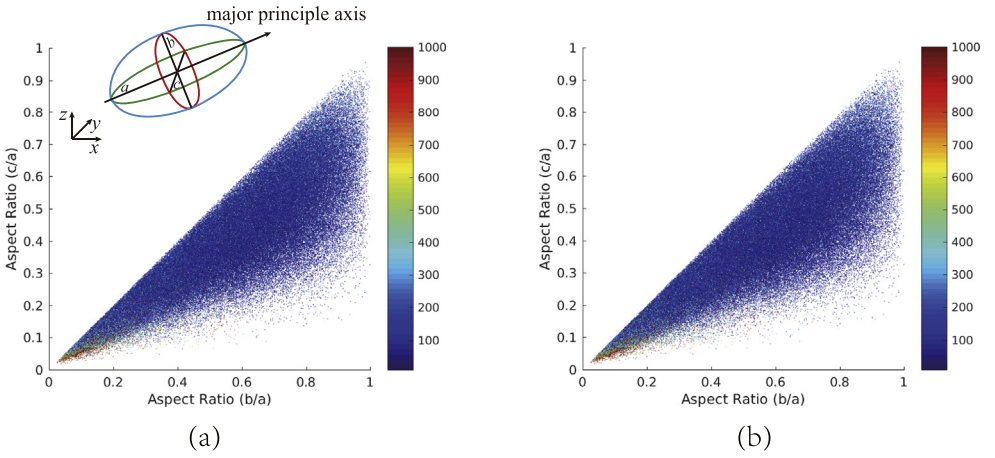

Fig. 21. Aspect ratios of individual grains from the simulation: (a) B1 case with unidirectional raster pattern; (b) B2 case with bidirectional raster pattern.

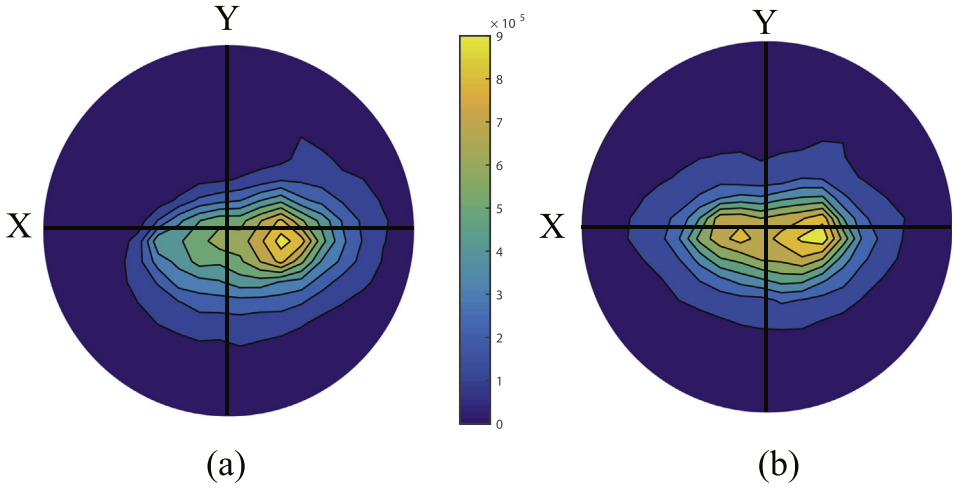

Fig. 22. Pole figures of grain shape orientations from the simulation: (a) B1 case with unidirectional scan direction; (b) B2 case with bidirectional scan direction.

CRediT authorship contribution statement

Yanping Lian: Conceptualization, Methodology, Formal analysis, Validation, Writing - original draft, Funding acquisition. **Zhengtao Gan:** Data curation, Visualization, Writing - original draft. **Cheng Yu:** Data curation, Writing - review & editing. **Dmitriy Kats:** Writing - review & editing. **Wing Kam Liu:** Supervision, Writing - review & editing. **Gregory J. Wagner:** Supervision, Methodology, Writing - review & editing.

Acknowledgments

This work was supported by the Beijing Institute of Technology Teli Young Fellow Recruitment Program, and in part by National Science Foundation (NSF) Cyber-Physical Systems (CPS) under Grant No. CPS/CMMI-1646592 and by the Center for Hierarchical Materials Design (CHiMaD) under grant no. 70NANB14H012.

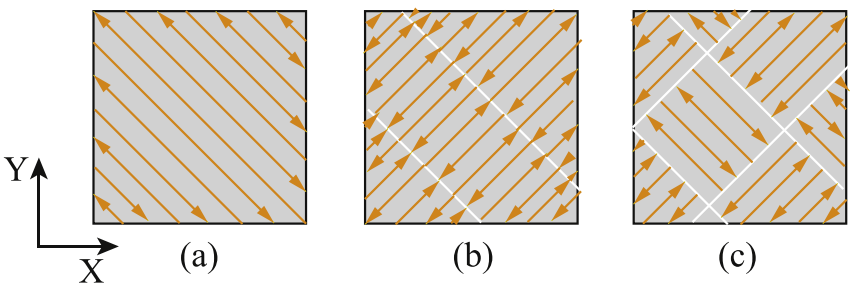

Fig. 23. Raster patterns in-layer: (a) meander pattern, (b) stripe pattern, and (c) chessboard pattern, where the arrow line stands for the scan direction.

Appendix A. Epitaxial grain growth model

In this appendix, we introduce a geometrical-based method to model the epitaxial grain growth mechanism. Epitaxial grain growth occurs at the contact surface (denoted Γ) between the region of melted material (denoted Ω^m) and the region of unmelted substrate (denoted Ω^s) for each continuous track. It is clear that $\Gamma = \Omega^m \cap \Omega^s$. During the solidification process, we select the unmelted cells close to the surface Γ, and "reactivate" the grain associated with each selected cell if the cell's temperature is above the solidus temperature.

Appendix B. Lipton-Glicksman-Kurz model

The undercooling itself includes four contributions: $\Delta T = \Delta T_t + \Delta T_c + \Delta T_r + \Delta T_k$ where ΔT_c, ΔT_t, ΔT_k and ΔT_r denote the undercooling contributions associated with solute diffusion, thermal diffusion, attachment kinetics and solid-liquid interface curvature, respectively. The growth kinetics of both columnar and equiaxed morphologies are calculated with the aid of the Lipton-Glicksman-Kurz (LGK) model [32]. In the LGK model, the first three undercooling terms above are taken into account, while we assume that the undercooling associated with attachment kinetics is neglected. Rather than giving a detailed description of the LGK model (which can be found in References [32,46]), the relationships used to describe the interplay of the dendrite tip radius, R, the dendrite tip velocity, v, and the three undercooling terms are presented here.

The formula for the thermal undercooling is given as

$$\Delta T_t = \frac{\Delta H}{c_p} \mathrm{Iv}(P_t) \tag{B1}$$

where ΔH is the latent heat and c_p represents the specific heat. The variable P_t is thermal Peclet number and defined as $P_t = vR/(2a)$ where a is the thermal diffusivity. The Ivantsov function is $\mathrm{Iv}(P) \equiv P\exp(P)E_1(P)$ with $E_1(P)$ the exponential integral function. The expression for the solute undercooling is

$$\Delta T_c = mC_0 \left[1 - \frac{1}{1-(1-k_0)\mathrm{Iv}(P_c)}\right] \tag{B2}$$

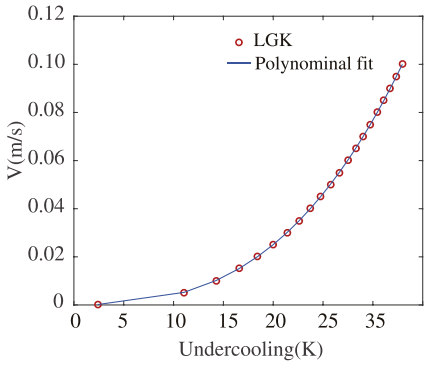

Fig. B.24. Growth kinetics of a dendrite tip, as calculated using the LGK model and fitted with a polynomial of degree 3, for IN718 alloy.

where m is the liquidus slope (assumed to be constant), C_0 is the initial alloy composition, k_0 is the equilibrium partition coefficient and here it is assumed that the solute trapping effects are ignored. The solute Peclet number is $\Delta P_c = vR/(2D)$ with D the liquid diffusion coefficient. The formula for the ΔT_r is

$$\Delta T_r = \frac{2\Gamma}{R} \tag{B3}$$

where Γ is the Gibbs-Thomson parameter (namely the ratio of the solid-liquid interface energy to the melting entropy). The relationship between R and v is described by

$$R = \frac{\Gamma\sigma^*}{\frac{P_t\Delta H}{c_p} - \frac{P_c m C_0(1-k_0)}{1-(1-k_0)\mathrm{Iv}(P_c)}} \tag{B4}$$

where σ^* is a stability constant and taken as $1/4\pi^2$[32].

Based on Eqs. (B1), (B2), (B3), and (B4) above, the dendrite tip velocity, v, as a function of $\Delta T = \Delta T_t + \Delta T_c + \Delta T_r$ can be uniquely calculated. In Fig. B.24, the growth rate of the dendrite tip for IN718 alloy is plotted for a given range of undercooling, while the corresponding parameter values are summarized in Table B.6. In order to save computational time, a cubic polynomial is used to fit the relationship of theoretical velocity and undercooling in the CA model:

$$v(\Delta T) = \lambda_1 \cdot \Delta T + \lambda_2 \cdot \Delta T^2 + \lambda_3 \cdot \Delta T^3 \tag{B5}$$

where the values of the coefficients λ_1, λ_2, and λ_3 corresponding to the fitting curve shown in Fig. B.24 are provided in Table 4.

Note that the IN718 alloy has been approximated by a pseudo-binary, Ni-Nb, and that the concentration and diffusion coefficients in the table refer to the properties of Nb in IN718 alloy.

References

[1] I. Tabernero, A. Lamikiz, S. Martínez, E. Ukar, J. Figueras, Evaluation of the mechanical properties of Inconel 718 components built by laser cladding, International Journal of Machine Tools and Manufacture 51 (6) (2011) 465–470.
[2] S. Copley, R. Martukanitz, W. Frazier, M. Rigdon, Mechanical properties of parts formed by laser additive manufacturing, Advanced Materials & Processes 169 (9) (2011) 26–29.
[3] K.N. Amato, S.M. Gaytan, L.E. Murr, E. Martinez, P.W. Shindo, J. Hernandez, S. Collins, F. Medina, Microstructures and mechanical behavior of Inconel 718 fabricated by selective laser melting, Acta Materialia 60 (5) (2012) 2229–2239.
[4] F. Liu, X. Lin, G. Yang, M. Song, J. Chen, W. Huang, Microstructure and residual stress of laser rapid formed Inconel 718 nickel-base superalloy, Optics & laser technology 43 (1) (2011) 208–213.
[5] L.L. Parimi, G.A. Ravi, D. Clark, M.M. Attallah, Microstructural and texture development in direct laser fabricated IN718, Materials Characterization 89 (2014) 102–111.
[6] J. Martin, B. Yahata, J. Hundley, J. Mayer, T. Schaedler, T. Pollock, 3D printing of high-strength aluminium alloys, Nature 549(7672) (2017) 365.
[7] M. Rappaz, C.-A. Gandin, Probabilistic modelling of microstructure formation in solidification processes, Acta metallurgica et materialia 41 (2) (1993) 345–360.
[8] D. Juric, G. Tryggvason, A front-tracking method for dendritic solidification, Journal of computational physics 123 (1) (1996) 127–148.
[9] W. Boettinger, J. Warren, C. Beckermann, A. Karma, Phase-field simulation of solidification, Annual Review of Materials Research 32 (1) (2001) 163–194.
[10] T.M. Rodgers, J.D. Madison, V. Tikare, Simulation of metal additive manufacturing microstructures using kinetic Monte Carlo, Computational Materials Science 135 (2017) 78–89.
[11] C.-A. Gandin, M. Rappaz, A 3D cellular automaton algorithm for the prediction of dendritic grain growth, Acta Materialia 45 (5) (1997) 2187–2195.

Table B.6
Properties of IN718 alloy [47].

c_p	435 $\mathrm{Jkg^{-1}K^{-1}}$	ΔH	1.52×10^5 $\mathrm{Jkg^{-1}}$	a	2.0779×10^{-6} $\mathrm{m^2t^{-1}}$	Γ	3.65×10^{-7} km
D	$3 \times 10^{-9}\mathrm{m^2s^{-1}}$	m	−10.5 K% $^{-1}$	k_0	0.48		

[12] H. Yin, S. Felicelli, Dendrite growth simulation during solidification in the LENS process, Acta Materialia 58 (4) (2010) 1455–1465.
[13] J. Zhang, F. Liou, W. Seufzer, K. Taminger, A coupled finite element cellular automaton model to predict thermal history and grain morphology of Ti-6Al-4V during direct metal deposition (DMD), Additive Manufacturing 11 (2016) 32–39.
[14] A. Rai, M. Markl, C. Körner, A coupled Cellular Automaton-Lattice Boltzmann model for grain structure simulation during additive manufacturing, Computational Materials Science 124 (2016) 37–48.
[15] A. Dezfoli, W. Hwang, W. Huang, T. Tsai, Determination and controlling of grain structure of metals after laser incidence: theoretical approach, Scientific Reports 7 (2017) 41527.
[16] C. Panwisawas, C. Qiu, M. Anderson, Y. Sovani, R. Turner, M. Attallah, J. Brooks, H. Basoalto, Mesoscale modelling of selective laser melting: thermal fluid dynamics and microstructural evolution, Computational Materials Science 126 (2017) 479–490.
[17] J. Koepf, M. Gotterbarm, M. Markl, C. Korner, 3D multi-layer grain structure simulation of powder bed fusion additive manufacturing, Acta Materialia 152 (2018) 119–126.
[18] X. Li, W. Tan, Numerical investigation of effects of nucleation mechanisms on grain structure in metal additive manufacturing, Computational Materials Science 153 (2018) 159–169.
[19] V. Manvatkar, A. De, T. DebRoy, Heat transfer and material flow during laser assisted multi-layer additive manufacturing, Journal of Applied Physics 116 (12) (2014) 124905.
[20] Z. Gan, H. Liu, S. Li, X. He, G. Yu, Modeling of thermal behavior and mass transport in multi-layer laser additive manufacturing of Ni-based alloy on cast iron, International Journal of Heat and Mass Transfer 111 (2017) 709–722.
[21] Z. Gan, G. Yu, X. He, S. Li, Numerical simulation of thermal behavior and multicomponent mass transfer in direct laser deposition of Co-base alloy on steel, International Journal of Heat and Mass Transfer 104 (2017) 28–39.
[22] Z. Gan, G. Yu, X. He, S. Li, Surface-active element transport and its effect on liquid metal flow in laser-assisted additive manufacturing, International Communications in Heat and Mass Transfer 86 (2017) 206–214.
[23] Y. Lee, M. Nordin, S. Babu, D. Farson, Influence of fluid convection on weld pool formation in laser cladding, Welding Journal 93 (8) (2014) 292S–300S.
[24] G. Pottlacher, H. Hosaeus, B. Wilthan, E. Kaschnitz, A. Seifter, Thermophysical properties of solid and liquid Inconel 718, Thermochimica Acta 382 (1-2) (2002) 255–267.
[25] R.I. Issa, Solution of the implicitly discretized fluid flow equations by operator-splitting, Journal of Computational Physics 62 (1985) 40–65.
[26] P.J. Oliveira, R.I. Issa, An improved PISO algorithm for the computation of buoyancy-driven flows, Numerical Heat Transfer, Part B 40 (2001) 473–493.
[27] C.-A. Gandin, M. Rappaz, A coupled finite element-cellular automaton model for the prediction of dendritic grain structures in solidification processes, Acta metallurgica et materialia 42 (7) (1994) 2233–2246.
[28] G.P. Dinda, A.K. Dasgupta, J. Mazumder, Laser aided direct metal deposition of Inconel 625 superalloy: microstructural evolution and thermal stability, Materials Science and Engineering: A 509 (1) (2009) 98–104.
[29] E. Chlebus, K. Gruber, B. Kuźnicka, J. Kurzac, T. Kurzynowski, Effect of heat treatment on the microstructure and mechanical properties of Inconel 718 processed by selective laser melting, Materials Science and Engineering: A 639 (2015) 647–655.
[30] Y. Lian, S. Lin, W. Yan, W.K. Liu, G.J. Wagner, A parallelized three-dimensional cellular automaton model for grain grwoth during additive manufacturing, Computational Mechanics 61 (2018) 543–558.
[31] C. Thompson, J. Floro, H. Smith, Epitaxial grain growth in thin metal films, Journal of applied physics 67 (9) (1990) 4099–4104.
[32] J. Lipton, M. Glicksman, W. Kurz, Dendritic growth into undercooled alloy melts, Materials Science and Engineering 65 (1984) 57–63.
[33] W. Kurz, B. Giovanola, R. Trivedi, Theory of microstructural development during rapid solidification, Acta metallurgica 34 (5) (1986) 823–830.
[34] A. Zinoviev, O. Zinovieva, V. Ploshikhin, V. Romanova, R. Balokhonov, Evolution of grain structure during laser additive manufacutring. Simulation by a cellular automata method, Materials and Design 106 (2016) 321–329.
[35] C.-A. Gandin, M. Rappaz, R. Tintillier, Three-dimensional probabilistic simulation of solidification grain structures: application to superalloy precsision castings, Metallurgical Transactions A 24 (1993) 467–479.
[36] J. Bragard, A. Karma, Y.H. Lee, Linking phase-field and atomistic simulations to model dendritic solidification in highly undercooled melts, interface Science 10 (2002) 121–136.
[37] T. Belytschko, W.K. Liu, B. Moran, K. Elkhodary, Nonlinear Finite Elements for Continua and Structures, John wiley & sons. 2013.
[38] M. Groeber, M. Jackson, DREAM. 3D: a digital representation environment for the analysis of microstructure in 3D, Integrating Materials and Manufacturing Innovation 3 (1) (2014) 5.
[39] H. Hosaeus, A. Seifter, E. Kaschnitz, G. Pottlacher, Thermophysical properties of solid and liquid Inconel 718 alloy, High Temperatures High Pressures(UK) 33 (4) (2001) 405–410.
[40] A. HasÃğalÃśk, M. Ay, CO2 laser cut quality of Inconel 718 nickel-based superalloy, Optics & Laser Technology 48 (2013) 554–564.
[41] P.N. Quested, J.J. Valencia, Modeling for casting and solidification processing, Thermophysical properties (2001) 189.
[42] P. Sahoo, T. DebRoy, M.J. McNallan, Surface tension of binary metal surface active solute systems under conditions relevant to welding metallurgy, Metallurgical transactions B 19 (3) (1988) 483–491.
[43] A. Kumar, S. Roy, Effect of three-dimensional melt pool convection on process characteristics during laser cladding, Computational Materials Science 46 (2009) 495–506.
[44] T. DebRoy, H. Wei, J. Zuback, T. Mukherjee, J. Elmer, J. Milewski, A. Beese, A. Wilson-Heid, A. De, W. Zhang, Additive manufacturing of metallic components-process, structure and properties., Progress in Materials Science 92 (2017) 112–224.
[45] J. Hunt, Steady state columnar and equiaxed growth of dendrites and eutectic, Materials Science and Engineering 65 (1) (1984) 75–83.
[46] J.A. Dantzig, M. Rappaz, Solidification, EPFL press, Lausanne. 2009.
[47] P. Nie, O. Ojo, Z. Li, Numerical modeling of microstructure evolution during laser additive manufacturing of a nickel-based superalloy, Acta Materialia 77 (2014) 85–95.